



Analysis on the Fatigue Properties of Shot-Peened Al-Si-Mg Alloy and Its Fatigue Life Prediction

Kaixin Su, Jiwang Zhang, Hang Li, Mingze Wu, Shoudong Zhu, Kejian Yi, and Jinxin Zhang

(Submitted February 20, 2020; in revised form July 8, 2020; published online August 12, 2020)

Ceramic micro-shot peening (CMSP) and steel micro-shot peening (SMSP) were utilized to investigate the effect of micro-shot peening (MSP) on the high-cycle fatigue properties of Al-7Si-0.3Mg casting aluminum alloy in a previous study. However, the improvement effects of CMSP and SMSP on the fatigue strength (at 5×10^7 cycles) were only 33% because the depth of harden layers was only 20 and 55 μm while the depth of compressive residual stress affected layers was only 37 and 68 μm . In this study, conventional shot peening (CSP) was utilized, and the results were compared with those of MSP, with the expectation that CSP would provide a greater improvement in the fatigue strength. The affected surface layers of the shot-peened specimens were characterized using surface morphology, microhardness, and residual stress analyses. In addition, the effect of CSP on the fatigue strength at 5×10^7 cycles was investigated using a rotating bending fatigue test ($R = -1$). An investigation of the extensive surface compressive residual stress relaxation process for the three different shot-peened specimens during cyclic loading was conducted using x-ray diffraction. In addition, the initiation sites for fatigue cracks on the fracture surface were observed using scanning electron microscopy. Furthermore, the fatigue life of the samples with the internal casting defect failure mode was predicted using linear elastic fracture mechanics, while that for samples with the surface crack initiation failure mode was predicted using the modified Morrow model considering the residual stress.

Keywords Al-7Si-0.3Mg, casting defects, fatigue fracture mechanism, life prediction, shot peening

1. Introduction

Al-7Si-0.3Mg casting aluminum alloy has been widely used in high-speed railway catenary positioning devices because of its good mechanical properties, castability, and corrosion resistance (Ref 1). Recently, as a result of the increasing speed of high-speed trains, the fatigue performance requirements for high-speed railway catenary positioning devices have also increased. Therefore, surface strengthening treatments, which are effective methods to improve the fatigue resistance of metallic materials, are widely applied to aluminum alloys to improve their fatigue performances (Ref 2-12).

Shot peening is one of the most widely used methods for mechanical surface strengthening treatment. In this method, the surface of a material or component is repeatedly bombarded by accelerated particles, which cause severe plastic deformation of the surface layer. This introduces work hardening and compressive residual stress on the substrate surface, which effectively improves the fatigue performance of the material or component. The effect of shot peening on the fatigue strength of a material is mainly due to the combination of the morphological integrity, compressive residual stress, and work

hardening of the surface layer (Ref 9-13). The optimal increase in fatigue strength after shot peening corresponds to a certain shot peening Almen strength, which depends on the properties of the shot-peened alloy. Therefore, numerous studies have been performed to find a method to achieve the greatest improvement in the fatigue performance (Ref 2-7). Benedetti et al. (Ref 2) studied the impact of shot peening on the bending fatigue behavior of Al-7075-T651 and analyzed the effects of modifications (roughness and work hardening) and of the residual stresses relaxation on fatigue properties. The results indicated that no significant residual stress relaxation was observed in samples tested at low loading levels. González et al. (Ref 3) studied the effects of severe shot peening, conventional shot peening, and composite shot peening on the fatigue behavior of 6063 aluminum alloy. The results indicated that severe shot peening introduced better grain refinement and residual stress than conventional shot peening. However, it significantly increased the surface roughness of the samples and produced defects, which adversely affected the improvement of the fatigue strength. In general (Ref 4), although conventional shot peening (CSP) introduces considerable compressive residual stress on the surface layer, the surface integrity will deteriorate and pits on the surface will easily initiate cracks. Micro-shot peening (MSP) technology is a new method of shot peening using micro-particles with a diameter of 0.02-0.2 mm. It not only introduces considerable compressive residual stress, but also guarantees a fine surface integrity (Ref 5-7). Several studies (Ref 5-7) have indicated that the value of surface compressive residual stress introduced by MSP treatment was about 50 MPa greater than that of CSP treatment, while the surface roughness of MSP treatment was only one-third to one-fifth of CSP treatment, resulting in that the fatigue life of MSP was around one order of magnitude greater than that of CSP treatment.

Kaixin Su, Jiwang Zhang, Hang Li, Mingze Wu, Shoudong Zhu, Kejian Yi, and Jinxin Zhang, State Key Laboratory of Traction Power, Southwest Jiaotong University, Chengdu 610031, China. Contact e-mail: zhangjiwang@swjtu.cn.

Residual stress can inhibit the initiation and propagation of cracks and is an important parameter for improving the fatigue strength (Ref 14, 15). However, studies have indicated that the compressive residual stress relaxes under external mechanical cyclic loading, leading to the reduction or even disappearance of the beneficial effects introduced by shot peening (Ref 4, 16). Many researchers (Ref 4, 16, 17) have reported a similar results that after the first cycle, a linear relationship between the residual stress and the logarithm of the number of cycles (1 cycle to eventual failure) could be observed. In order to describe the relaxation process of the residual stress quantitatively, Kodama (Ref 17) proposed the following relationship:

$$\sigma_r = A + m \log N \quad (\text{Eq 1})$$

where σ_r is the compressive residual stress after N cycles; and m and A are material constants and are related to the magnitude of the loading stress σ_a .

It is well known that, for casting aluminum alloys similar to Al-7Si-0.3Mg, due to internal casting defects such as shrinkage, oxides and inclusions, the location of fatigue crack nucleation was likely to occur in the internal casting defects rather than the sample surface, reducing the fatigue strength severely (Ref 18-22). Due to the existence of internal casting defects, the fatigue fracture mechanism of the material after surface strengthening may become complex and uncertain. Therefore, further study about shot peening on casting aluminum alloy is needed. The effects of CMSP and SMSP on the fatigue properties of Al-7Si-0.3Mg casting aluminum alloy were investigated in previous study (Ref 14), although the considerable surface integrity and compressive residual stress were obtained, due to the limited depth of the shot-peened layer, the inhibition of internal casting defects was also limited (Ref 23, 24). Therefore, the improved effects of CMSP and SMSP on fatigue strength were not satisfactory. Compared with MSP, CSP could obtain the deeper affected shot-peened layer of work hardening and of compressive residual stress (Ref 25-27), which could suppress the negative effect of deeper casting defects. Therefore, in order to further improve the fatigue performance of shot-peened Al-7Si-0.3Mg casting aluminum alloy, CSP was utilized compared with CMSP and SMSP conducted in the previous study (Ref 14). However, it should be noted that compared with MSP, the surface integrity of CSP was also significantly damaged, which also increased the probability of crack initiation and early failure of the samples, therefore the adverse effect on the fatigue strength of CSP could not be ignored. The influence of different shot-peened treatments on the fatigue strength and fracture mechanism of Al-7Si-0.3Mg casting aluminum alloy needs a further study. In addition, fatigue life predicted model of specimens with internal casting defects or surface crack initiation should be further developed.

The total fatigue life, N_f , of a specimen consists of the number of cycles, N_i , required for crack initiation and the number of cycles, N_p , required for crack propagation to final failure. In several studies (Ref 28-31), cracks were observed to grow from casting defects at or shortly after the first loading cycle. Gao et al. (Ref 32) also found that the crack "initiation life" for 7475-T7351 aluminum alloy was only a very small fraction of the total fatigue life. Thus, N_i was negligible relative to N_f . Therefore, it is reasonable to predict the fatigue life of structural components with defects using the LEFM method (Ref 28-31). Casting defects can be regarded as initial cracks with a certain length of a_i . Then, according to the crack growth

rate and fracture toughness of the material, the number of cycles from initial crack a_i to final a_f could be calculated simply using the Paris–Erdogon equation such as Eq 2, which shows crack growth life N_p (Ref 23).

$$\frac{da}{dN} = C(\Delta K_{\text{eff}})^m \quad (\text{Eq 2})$$

$$\Delta K = Y(a)\Delta\sigma\sqrt{\pi a} \quad (\text{Eq 3})$$

where ΔK_{eff} is the effective stress intensity factor range, which is equal to $U \cdot \Delta K$, and factor U is usually derived from the measurement of crack closure. Some studies (Ref 33-35) have shown that U was a function of R and a . When the loading stress and R were constant, U was only related to crack length a . Therefore, Eq 2-3 can be extended as following (Ref 21):

$$\frac{da}{dN} = CY(a)^m U_R(a)^m (\Delta\sigma)^m (\pi a)^{m/2} \quad (\text{Eq 4})$$

where $\Delta\sigma$ is the loading stress, and $Y(a)$ is the calibration factor. When the loading stress is constant, Eq 4 can be integrated as following (Ref 21):

$$\int_{a_i}^{a_f} \frac{da}{Y(a)^m U_R(a)^m (\pi a)^{m/2}} = C \cdot (\Delta\sigma)^m \int_{N_i}^{N_f} dN \quad (\text{Eq 5})$$

Compared with $(\pi a)^{m/2}$, $Y(a)^m$ and $U_R(a)^m$ make smaller contributions to the left integral. Thus, result of the left integral mainly depends on the small a . Therefore, in the integration process, it can be assumed that $Y(a) = Y(a_i) = a$ constant and $U_R(a) = U_R(a_i) = a$ constant, which will only produce a small error for the entire integration process. By substituting $N_p = N_f - N_i$ into the right formula after the integral, it is possible to easily obtain the following (Ref 23):

$$N_p = \frac{2a_i^{(2-m)/2}}{(m-2)CY(a_i)^m U_R(a_i)^m \pi^{m/2} (\Delta\sigma)^m} \quad (\text{Eq 6})$$

$$B = \frac{2}{(m-2)CY(a_i)^m U_R(a_i)^m \pi^{m/2}} \quad (\text{Eq 7})$$

Thus, after combining Eq 6 and 7, the following is obtained (Ref 23):

$$N_p = B(\Delta\sigma)^{-m} a_i^{(2-m)/2} \quad (\text{Eq 8})$$

According to these studies (Ref 28-31), it can be seen that the value of N_i required for crack initiation was negligible relative to total fatigue life N_f . Thus, crack growth life N_p calculated using Eq 8 is approximately equal to total fatigue life N_f . Therefore, Eq 8 can be written as a relationship involving three variables, total fatigue life N_f , loading stress σ_a , and initial crack length a_i , as shown in Eq 9 (Ref 23).

$$N_f = B\sigma_a^{-m} a_i^{(2-m)/2} \quad (\text{Eq 9})$$

Murakami and Endo (Ref 36-38) proposed the concept of projected defect area A_i , based on fracture analysis. A casting defect inducing fatigue failure could be regarded as the largest size defect on the fatigue fracture surface of a sample (Ref 39, 40). Assuming that the casting defect size was a random variable, it could be described by the cumulative distribution function. Different kinds of cumulative distribution functions were used to evaluate the sizes of the initial defects in metal

structures in a large number of studies (Ref 39–43). Tiryakioğlu (Ref 44) used seven different distribution functions to describe the maximum defect size after the fatigue fracture of an Al-7Si-0.3Mg specimen, and Gumbel and general extreme value (GEV) cumulative distribution functions were finally proposed based on the goodness of fit results.

In addition to internal casting defects for Al-7Si-0.3Mg, it was necessary to establish a fatigue life prediction model with the surface crack initiation. Based on the Manson–Coffin equation (Ref 45, 46), Morrow (Ref 47) proposed a modification relationship of the total strain life equation between the total strain amplitude and the number of loading cycles, while the elastic strain amplitude ε_e in the modification relationship considering the compressive residual stress on the surface after shot-peened treatments. The final form after the modification with the compressive residual stress is as follows:

$$\varepsilon_a = \varepsilon_e + \varepsilon_p = \frac{\sigma'_f - \sigma_r}{E} (2N_f)^b + \varepsilon'_f (2N_f)^c \quad (\text{Eq 10})$$

where ε_a is the total strain amplitude; ε_e is the elastic strain amplitude; E is Young's modulus for the material; σ'_f is the fatigue strength coefficient; b is the fatigue strength exponent; ε'_f is the fatigue ductility coefficient; c is the fatigue ductility exponent; N_f is the fatigue life; and σ_r is the compressive residual stress on the fatigue samples induced by different shot-peened treatments.

In this study, the S – N curve of CSP specimens was obtained using rotating bending fatigue tests ($R = -1$). The surface properties were also characterized using surface roughness, morphology, microhardness, and x-ray diffraction (XRD) measurements, along with microscopy observations. The evolution of the surface compressive residual stress variation during fatigue tests up to 5×10^7 cycles or failure was also comparatively investigated. Furthermore, the fatigue life of the samples with the internal casting defect failure mode was predicted using linear elastic fracture mechanics (LEFM), while that for samples with the surface crack initiation failure mode was predicted using the modified Morrow model considering the residual stress.

2. Experiment Materials and Methods

2.1 Materials

The material used in this study was Al-7Si-0.3Mg casting alloy, which was produced by gravity casting and subjected to T6 heat treatment. Its mechanical properties and chemical composition were characterized in our previous study (Ref 48). The yield strength, ultimate tensile strength, and elongation were 257.0, 310.5 MPa, and 6.4%, respectively. The chemical composition of the sample are Si (7.11%), Mg (0.369%), Mn (0.0042%), Fe (0.147%), Ni (0.009%), Zn (0.0068%), Ti (0.159%), Cr (0.032%), Cu (< 0.005), and Al (balance). The grain size was about 150 μm (Ref 49).

2.2 Shot Peening Conditions

The specimens used in fatigue tests were machined into the shape and dimensions shown in Fig. 1. The CSP and MSP (CMSP and SMSP) shot peening treatments were conducted using KSP-1000P and SGF-3 pneumatic shot peening machine. The shot-peened area was located in the middle hourglass area

shown in Fig. 1. Cast steel particles (S110) with a diameter of approximately 300 μm were used for CSP based on the recommendation in the ASM 2430 (Ref 50) standard for shot peening an aluminum alloy. The distance between the specimen and nozzle was approximately 150 mm. The Almen intensities after different shot peening treatments were calculated using the SAE J443 (Ref 51) standard, and the coverage values were estimated according to the SAE J2277 (Ref 52) standard. The shot peening parameters are listed in Table 1. The shot peening parameters for CMSP and SMSP were reported in (Ref 14).

2.3 Surface Morphology and Roughness

For measurement convenience, the surface roughness and morphology of each specimen were determined on the flat surfaces of small cylindrical samples with a diameter of 12 mm and a height of 10 mm treated by the same shot-peened condition as the fatigue samples. The surface morphology of each fatigue sample was observed using an OLMPUS OLS4100 confocal laser microscope, and the surface roughness values R_a , R_z and R_{max} along the axial direction were measured using an evaluation length of 12 mm. R_a , R_z , and R_{max} represent the arithmetic mean roughness, arithmetic mean of the distance between the peak and the valley, and maximum depth of the profile valley, respectively. Each value was the average of three measurements.

2.4 Microstructure and Cross Section Microhardness

In order to observe the in-depth microstructures of the shot-peened specimens, minimum cross section with a diameter of 12 mm which was normal to the axial direction was cut, polished, and, etched by a mixed acid solution containing 5 mlHF + 15 mlHCl + 25 mlHNO₃ + 955 mlH₂O. Afterward, an OLYMPUS GX71 optical microscope was used to observe the etched surface.

In addition, in order to obtain the in-depth microhardness values of the shot-peened samples, the cross sections of the samples were inlaid and polished. The Vickers hardness values of the specimens were determined using an HVS-1000Z microhardness tester at a load of 0.245 N and holding time of 10 s, and the mean values were calculated from three groups of data.

2.5 Residual Stress Measurement

The values of axial residual stress were measured using a Pustec μ -X360n instrument at the smallest cross section of the hourglass in the middle, and four points in the circumferential direction were measured and averaged to determine the final value. The relaxation processes for the compressive residual stress on the surfaces of the shot-peened samples were analyzed under the same loading stress amplitude (120 MPa). The tests were interrupted within a preset failure period to measure the residual stresses on the surfaces of the samples. The x-ray tube was operated at voltage and current values of 30 kV and 1.0 mA, respectively, using Cr-K α radiation. The elasticity modulus to obtain residual stresses was 69.310 GPa. The incident x-ray beam formed at an angle of 25° with the specimen axis, and the diffracted crystal surface was {311}. At the same time, the oscillation unit was set to obtain more information on the grains to obtain more accurate measurement values considering the grain coarseness on the surface of the aluminum alloy. The x-rays that were diffracted (from the

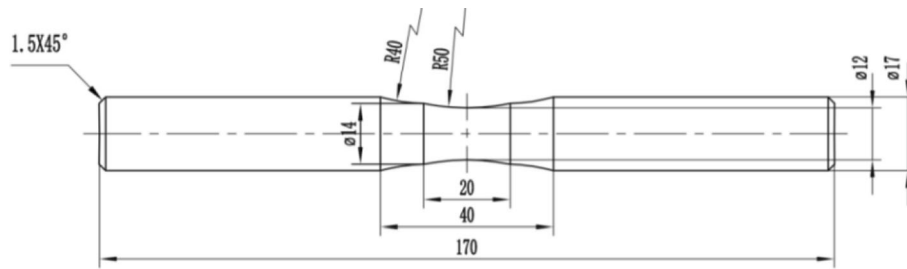
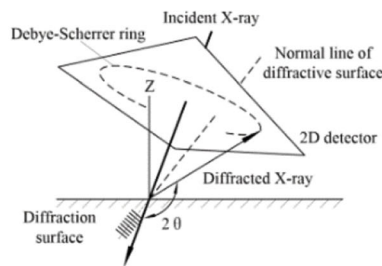


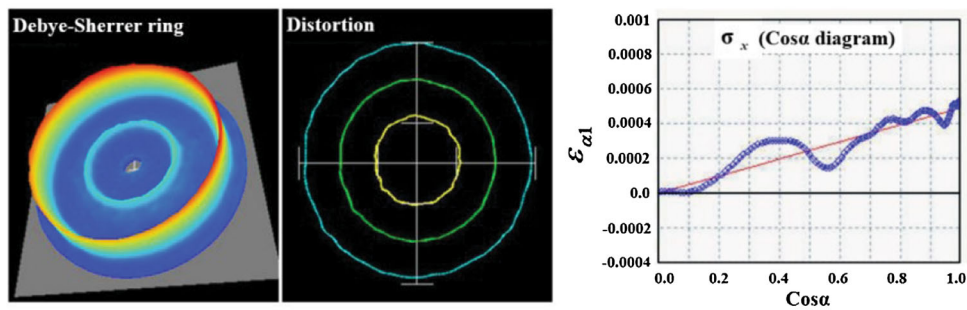
Fig. 1 Shape and dimensions of specimen used in four-point rotating bending fatigue test (all units in mm)

Table 1 Conditions of shot peening process (coverage: 300%)

Treatment	Particle diameters, μm	Air pressure, bar	Almen intensity
CSP	300	1.5	0.19 mmA
CMSP	50	4	0.12 mmN
SMSP	50	4	0.16 mmN



(a) X-ray diffraction measurement of Cos α method



(b) Debye–Sherrer ring (c) Distortion (d) Cos α diagram

Fig. 2 XRD measurement of residual stress

polycrystalline structure of the specimen) with a 360° omnidirectional diffraction angle were recorded using a 2D planar detector, which was perpendicular to the X incident beam, as shown in Fig. 2(a). The distortion at different angles (α) was then obtained from the Debye–Scherrer ring, as shown in Fig. 2(b), to calculate the strain, as shown in Fig. 2(c). Finally, the residual stress was calculated according to the Cos α method introduced by Lin (Ref 53), as shown in Fig. 2(d), using the calculation equations shown in Eq 11-13. The distributions of the residual stress in the depth direction of the surface layer for different shot-peened samples were obtained utilizing the

continuous electrolytic polishing method. In addition, the measured results were corrected utilizing the elastic solution reported by Moore and Evans (Ref 54), considering the redistribution of the stress due to the removal of surface material.

$$\varepsilon_{\alpha} = -\Delta\theta / \tan \theta (0 \leq \alpha \leq 2\pi) \quad (\text{Eq 11})$$

$$\varepsilon_{\alpha 1} = \{(\varepsilon_{\alpha} - \varepsilon_{\pi+\alpha}) + (\varepsilon_{-\alpha} - \varepsilon_{\pi-\alpha})\} / 2 \quad (\text{Eq 12})$$

$$\sigma_r = -\{E \cdot (\partial \varepsilon_{\alpha 1} / \partial \cos \alpha)\} / \{(1 + \nu) \cdot \sin 2\eta \cdot \sin 2\varphi_0\} \quad (\text{Eq 13})$$

where θ is the diffraction angle between the x-ray and crystal surface; ε_{α} , $\varepsilon_{\alpha 1}$, $\varepsilon_{\pi+\alpha}$, and $\varepsilon_{\pi-\alpha}$ are the strains at different angles of the Debye–Scherrer ring; E and ν are Young’s modulus and Poisson’s ratio for the material, respectively; η is the diffraction angle between the reflection line and the input x-ray; φ_0 is the azimuth between the normal of the sample and the input x-ray; and σ_r is the residual stress obtained using the $\text{Cos}\alpha$ method.

2.6 Fatigue Test

All of the specimens were tested at room temperature using a four-point rotating bending fatigue machine ($R = -1$, $f = 50$ Hz) at a constant amplitude load. The tests were based on the median $S-N$ method with a small sample size (Ref 55). The $S-N$ curves corresponding to a 50% failure probability were obtained using the least squares fitting method (Ref 55), which was based on the Origin software. The number of fatigue specimens was 5–10 at different stress amplitudes, and one or two specimens were used for each stress amplitude level. The test was terminated when the number of cycles reached 5×10^7 or the sample failed. All of the fracture surfaces of the specimens were observed using a JSM-6610LV scanning electron microscopy (SEM) instrument to identify the fatigue fracture behavior.

3. Result

3.1 Surface Roughness and Morphology

The surface roughness values of different treated samples are shown in Table 2. It can be seen that the surface roughness values significantly increased after shot peening, and the values for the CSP samples were significantly higher than those for the un-peened (UP) sample and the other two MSP samples.

3.2 Surface Microhardness Distribution and Cross Section Microstructure

The cross section microstructures of three different shot-peened samples are shown in Fig. 3. It can be seen CSP and MSP caused different degrees of plastic deformation on the surfaces of the samples. A plastic deformation layer with an average thickness of approximately $70 \mu\text{m}$ existed on the surface of the CSP sample. Plastic deformation layers could also be observed after CMSP and SMSP, but the thicknesses were smaller, at approximately 10 and $30 \mu\text{m}$, respectively. This indicated that compared to MSP, CSP could introduce a deeper plastic deformation layer on the surface of the sample. For MSP, SMSP could introduce a deeper plastic deformation layer than CMSP under the same shot peening air pressure.

The in-depth microhardness distributions of three shot-peened samples are illustrated in Fig. 4. It can be seen that the three different shot peening treatments all introduced a hardened layer on the surface of the sample. As the depth of

Table 2 Surface roughness values and statistics on failure modes of four different treated specimens

	$R_a, \mu\text{m}$	$R_z, \mu\text{m}$	$R_{\text{max}}, \mu\text{m}$	Internal casting defects	Surface crack initiation
UP	0.08	0.47	0.54	2	7
CSP	5.13	30.33	49.60	0	6
CMSP	0.79	4.13	27.00	4	0
SMSP	3.90	28.67	101.72	2	4

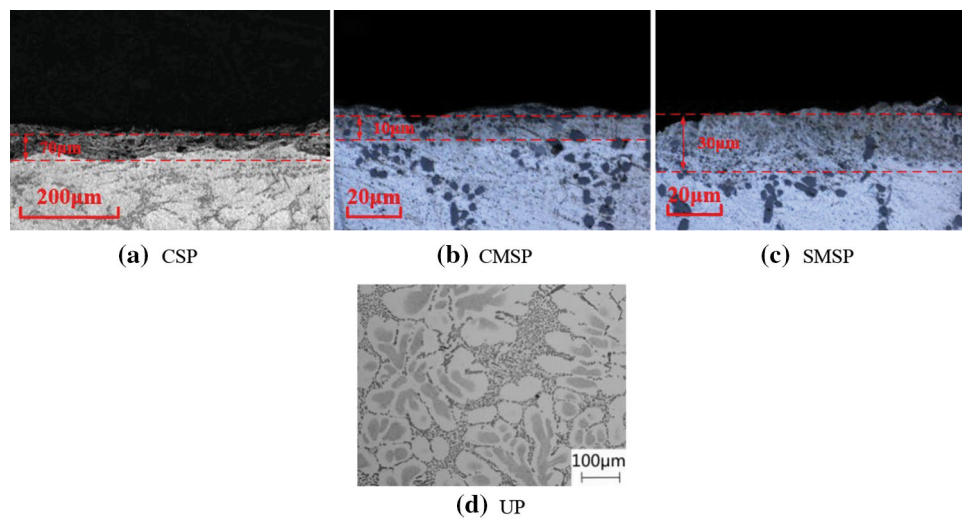


Fig. 3 Microstructure observations

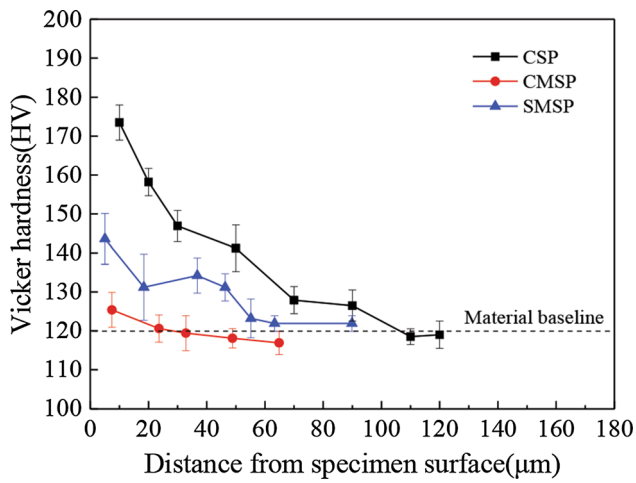


Fig. 4 In-depth microhardness distributions of different shot-peened specimens

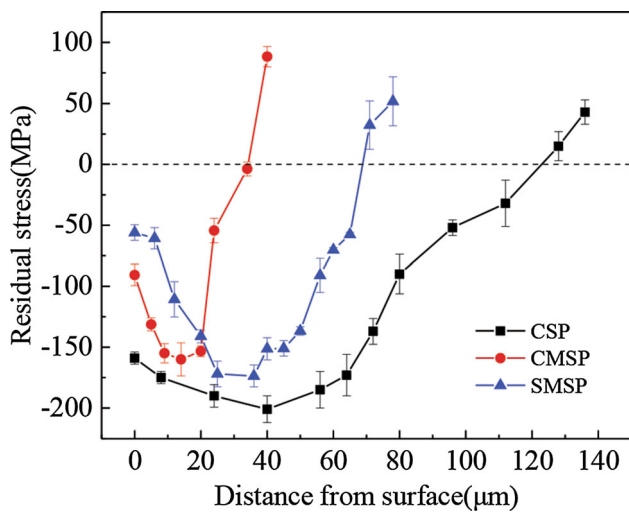


Fig. 5 Distributions of compressive residual stress near surfaces of shot-peened specimens

the profile increased, the microhardness gradually decreased. The dashed line indicates that the microhardness of the base metal was approximately 120 HV. After shot peening, the microhardness values of the CSP, CMSP, and SMSP samples were approximately 174, 126, and 144 HV at 10, 8, and 5 μm from the surface, respectively. The depths of the hardened layer were approximately 100, 20, and 55 μm , respectively.

3.3 Surface Residual Stress Distribution

The distributions of axial residual stress in the depth direction of the sample surfaces are illustrated in Fig. 5. It can be seen that layers with compressive residual stress were introduced on the sample surfaces by the three different shot-peened treatments. The values of compressive residual stress on the surfaces of the CSP, CMSP, and SMSP samples were -159 , -91 , and -56 MPa, respectively, and the depths of the affected layers were approximately 123, 37, and 68 μm , respectively. The maximum compressive residual stresses were -201 MPa at a depth of approximately 40 μm for the CSP specimens, -160 MPa at a depth of 14 μm for the CMSP specimens, and -174 MPa at a depth of 36 μm for the SMSP

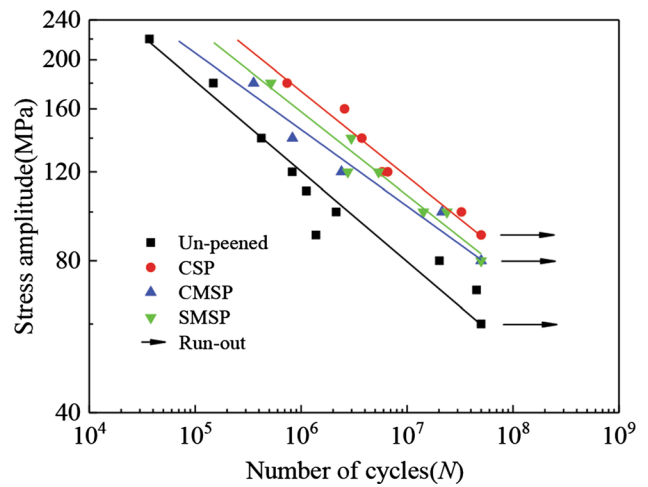


Fig. 6 $S-N$ curves

specimens. All UP specimen surfaces were electropolished to remove the machined influence of residual stress and hardening layer on fatigue properties before fatigue test. The surface residual stress of UP sample after electropolishing was -8 MPa. From the above, compared with the two different MSP treatments, the CSP introduced a larger compressive residual stress on the sample surface and the maximum compressive residual stress in the depth direction. In addition, the depth of the affected layer was also greater.

3.4 $S-N$ Curve

The $S-N$ curves corresponding to a 50% failure probability (Ref 55) are shown in Fig. 6. When the loading stress was high (180 MPa), the fatigue lives of all the samples had a 10^5 order of magnitude, and the fatigue life of the CSP sample was the highest, with a value that was approximately 5 times higher than that of the UP sample, and approximately 1-2 times higher than those of the CMSP and SMSP samples. When the loading stress was low (100 MPa), the fatigue life of the CSP sample was approximately 15 times higher than that of the UP sample, and the increase was more obvious than that with a high stress. The CSP treatment used in this study improved the fatigue strengths of the samples, and the improvement was more obvious than those with CMSP and SMSP. The fatigue limit of the UP sample at 5×10^7 cycles was 60 MPa, while those of the CSP, CMSP, and SMSP specimens increased to 90, 80, and 80 MPa, and the corresponding increase percentages were 50, 33, and 33%, respectively.

3.5 Fracture Surface Observation

The SEM fracture surface images of different treated samples are shown in Fig. 7. It can be seen that two failure modes were observed: internal casting defects and surface crack initiation. The statistics for these failure modes are listed in Table 2. It can be seen from Table 2 that there were also two failure modes (internal casting defects and surface crack initiation) for the UP specimens. As stated in Sects. 3.1–3.3, the CSP specimens had a deeper layer affected by the shot peening, which inhibited the deeper casting defects. In addition, because the surface roughness was larger, only the surface crack initiation failure mode could be observed. Because of the large compressive residual stress and small roughness values on the surfaces of the CMSP specimens, the crack initiation from

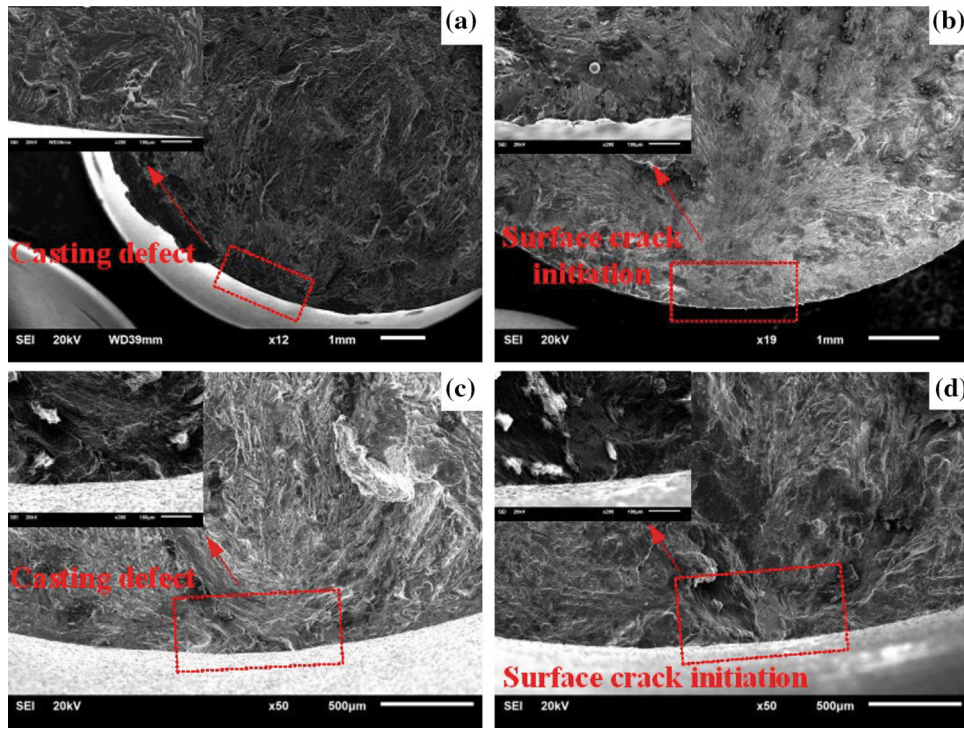


Fig. 7 Observation of crack initiation sites of different treated specimens: (a) UP: $\sigma_a = 70$ MPa; (b) CSP: $\sigma_a = 100$ MPa; (c) CMSP: $\sigma_a = 180$ MPa; (d) SMSP: $\sigma_a = 140$ MPa

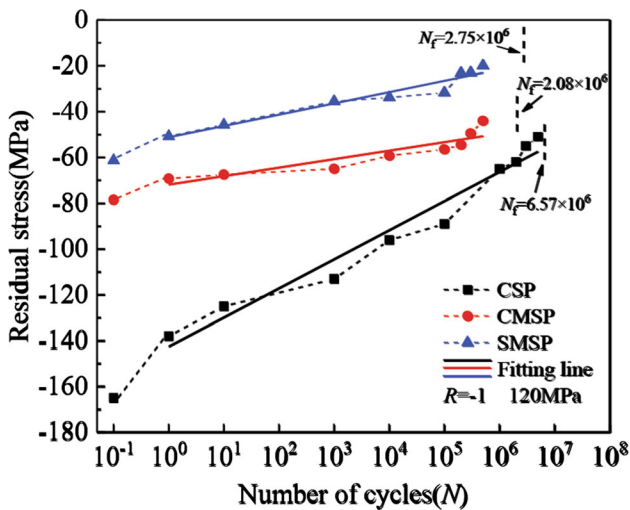


Fig. 8 Comparison of relaxation processes in different shot-peened specimens

the surface could be effectively inhibited. In addition, the layer affected by CMSP was shallow, and the ability to inhibit internal casting defects was not significant. Thus, only the internal casting defect failure mode could be observed. Compared with CMSP, SMSP introduced a deeper shot peening affected layer, but also obviously increased the roughness values. Therefore, the competition between internal casting defects and surface crack initiation in the SMSP specimens resulted in a difference in the failure modes. In conclusion, the differences in the residual stress, depth of the affected layer, and roughness introduced by the different shot-peened treatments caused a change in the fatigue fracture mechanism.

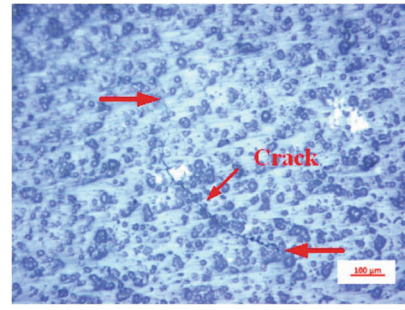
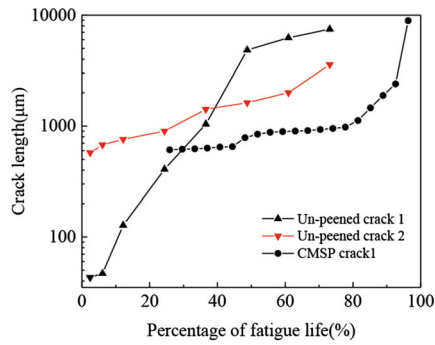
3.6 Residual Stress Relaxation Process

The results as shown in Fig. 8 indicated that the compressive residual stress on the surface gradually decreased with an increase in the cycles. The relaxation process for the compressive residual stress of the CSP sample was significantly faster than those of the other two different MSP samples. It was because that the initial compressive residual stress of the CSP sample was considered to be significantly larger than those of the two MSP specimens, and the actual loading stress of the CSP sample caused by the larger roughness was also larger than that of the MSP specimen, which was similar to the results reported by Li et al. (Ref 4). In addition, the residual stresses of two different MSP samples and CSP sample were measured before and after the fatigue tests under a stress amplitude of 80 and 90 MPa (unbroken at 5×10^7 cycles). The results indicated that there were almost no relaxation of residual stress (CMSP: from -87 to -86 MPa, SMSP: -55 to -54 MPa) before and after fatigue tests in the two MSP samples. However, there was an obvious relaxation of residual stress (from -159 to -84 MPa) before and after fatigue test in the CSP sample. In addition, it could also be seen that during the first cycle of the load, the residual stress relaxed significantly. After the first cycle, a linear relationship between the residual stress and the logarithm of the number of cycles (1 cycle to eventual failure) could be observed, and many researchers have reported similar results (Ref 4, 16, 17). Consequently, the following empirical equations could be used to quantitatively describe the relaxation process for three different shot-peened samples under loading stress according to Kodama (Ref 17).

For CSP specimens:

$$\sigma_r(N) = 12.70 \log N - 142.54; \quad (\text{Eq 14})$$

For CMSP specimens:



(a) Crack propagation processes in UP and CMSP samples (b) Replica image of CMSP sample, $N=1400000$ cycles

Fig. 9 Crack propagation behavior

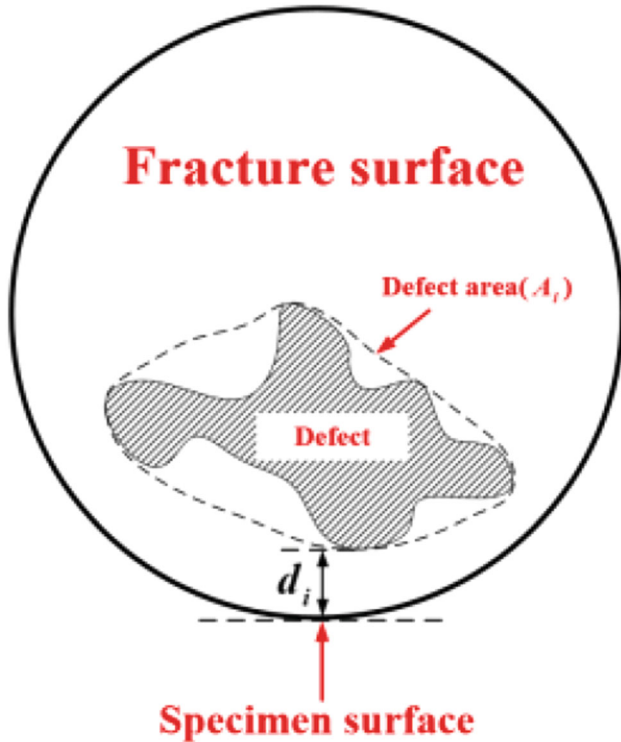


Fig. 10 Projected casting defect area A_i

$$\sigma_r(N) = 3.71 \log N - 71.87; \quad (\text{Eq 15})$$

For SMSP specimens:

$$\sigma_r(N) = 4.93 \log N - 51.14; \quad (\text{Eq 16})$$

where σ_r is the surface residual compressive stress after N cycles; N is the number of cycles ($1 \leq N \leq 5 \times 10^7$).

4. Discussion

4.1 Fatigue Life Prediction Based on Linear Elastic Fracture Mechanics

4.1.1 Crack Growth Behavior. The surface crack propagation behaviors of the UP and CMSP specimens under a loading stress of 120 MPa were also studied using crack

replicating technology (Ref 14, 48), as shown in Fig. 9(a). The crack replica image of CMSP specimen is shown in Fig. 9(b). The results showed that at the first interruption test (accounting for 2.4% of the total fatigue life), main cracks 1 and 2 with lengths of 43 and 574 μm , respectively, had appeared on the surface of the UP specimen. Similarly, in the first interruption test (accounting for 25.9% of the total fatigue life), main crack 1 with a length of 610 μm appeared on the surface of the CMSP specimen. Although the CSP and SMSP samples were limited by their large surface roughness values, which prevented crack replication, it was easy to determine that the number of cycles, N_i , required for crack initiation was negligible relative to the total fatigue life, N_f , which also confirmed that the assumption of $N_i \approx 0$ in the literature (Ref 28-31) was reasonable.

4.1.2 Cumulative Distribution Function of Defect Size.

The concept of projected defect area A_i based on fracture analysis is shown in Fig. 10. Here, d_i is the distance between the casting defects and free surface of the samples, and a_i can be equivalent to $\sqrt{A_i}$ (Ref 37). After a rotating bending fatigue test, values for $\sqrt{A_i}$ on the fractures of the fatigue specimens caused by casting defects were obtained, and initial crack length a_i was defined as $\sqrt{A_i}$. For Al-7Si-0.3Mg alloy, the descriptive statistics on initial crack length (a_i) based on 8 samples are: 99 μm (mean), 201 μm (max), 32 μm (min), and 87 μm (median).

The values for initial crack length a_i were arranged according to size, where $a_i < a_{i+1}$ and n was the number of fatigue failure samples caused by casting defects. Then, the probability of not exceeding a_i can be described by a mean rank equation (Ref 56).

$$F(a_i) = \frac{i}{n + 1} \quad (\text{Eq 17})$$

According to the suggestion of Tiryakioğlu (Ref 44), the experimental data were fitted using two cumulative distribution functions (Gumbel and GEV). In addition, the Weibull and generalized Pareto (GP) cumulative distribution functions were used to fit the experimental data based on Origin software, and the goodness of fit results of the four different cumulative distribution functions were compared and analyzed. The parameter values, goodness of fit results, and values of estimated initial crack length a_i when the failure probability was 99% for each distribution function are listed in Table 3, and the fitting curves are shown in Fig. 11. It can be seen that all four different distribution functions used in this study could provide considerable goodness of fit results, and the GEV

Table 3 Estimated parameters for the distributions

Distribution	Cumulative probability function	Parameter	Value	R^2	a_i (μm) – $F(a_i) = 99\%$
Gumbel	$F(a_i) = \exp(-\exp(-\frac{a_i-\lambda}{\delta}))$	λ	72.24	0.970	292.3
GEV	$F(a_i) = \exp(-(1 + \xi(\frac{a_i-\lambda}{\delta})^{-\frac{1}{\xi}}))^{-\xi}$	δ	47.95	0.976	269.9
		λ	71.57		
Weibull	$F(a_i) = 1 - \exp(-(\frac{a_i}{\delta})^\xi)$	δ	43.94	0.965	409.5
		ξ	0.207		
		ξ	1.727		
GP	$F(a_i) = 1 - (1 + \xi(\frac{a_i-\lambda}{\delta})^{-\frac{1}{\xi}})$	λ	24.83	0.960	273.4
		δ	103.7		
		ξ	-0.328		

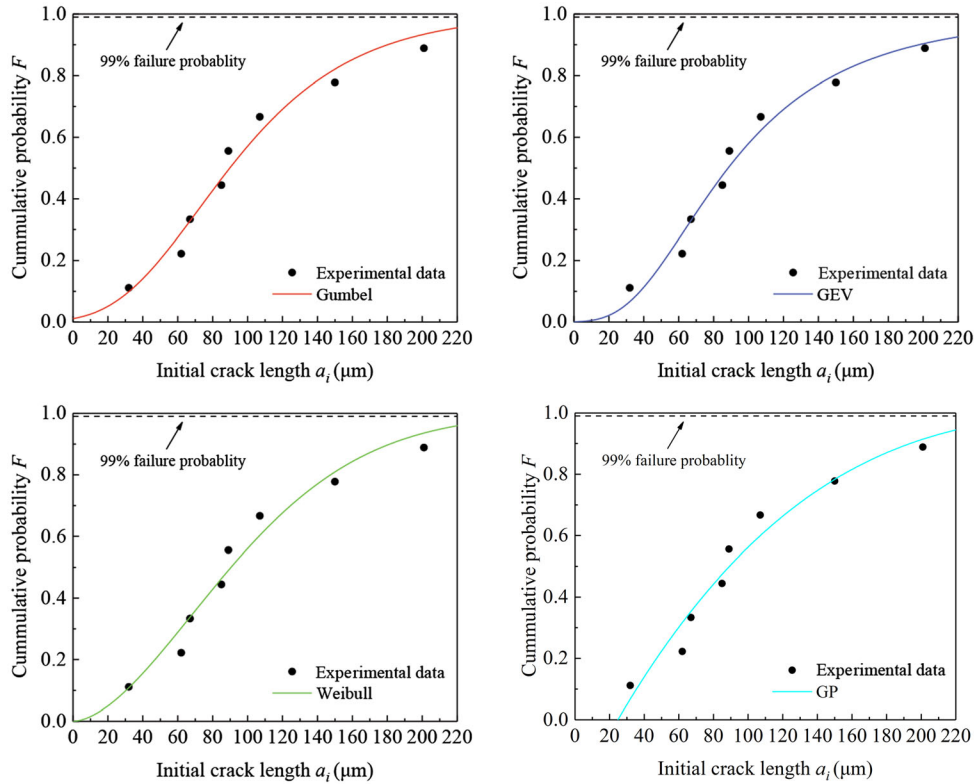


Fig. 11 Cumulative probability plot for data and Gumbel, GEV, Weibull, and GP fitting results

distribution was slightly better than the other three. When the failure probability was 99%, the most conservative estimation of initial crack length a_i could be obtained using the Weibull distribution. However, there was no significant difference between the initial crack length a_i values estimated by the other three distribution functions.

4.1.3 Fatigue Life Prediction for Samples with Internal Casting Defects. Equation (9) is a simple method for estimating the fatigue life based on the loading stress and size of the casting defects. A linear relationship of $\log A_i - \log N_f$ was fitted under a constant stress by analyzing the Al-7Si-0.3Mg aluminum alloy fatigue test data (Ref 44, 57). Thus, the values of B and m in Eq 9 were equal to 1.827×10^{17} and 4.246, respectively. Because a large amount of experimental data is needed to determine the values of B and m , and the chemical

compositions and mechanical properties of the material used in this study were similar to the alloys considered in (Ref 44, 57), they could be used for this research. The values of the distance, d_i , between the casting defects and the free surface for all the fatigue specimens were calculated, and the actual loading stress at the casting defects causing fatigue failure were converted according to nominal loading stress σ_a and d_i . The fatigue lives of specimens with casting defects were predicted using Eq 9, as shown in Fig. 12. It can be seen that there was an obvious law in the predicted results for the UP, CMSP, and SMSP specimens. The predicted results for the UP samples were slightly greater than the experimental results, whereas the predicted results for the CMSP and SMSP samples were both slightly smaller than the experimental results. This was due to neglecting the inhibition effect of the shot-peened layers on the

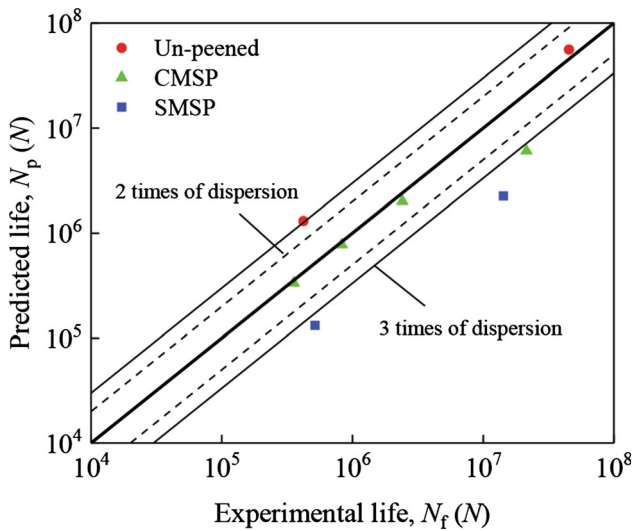


Fig. 12 Comparison of predicted and experimental fatigue lives based on LEFM model

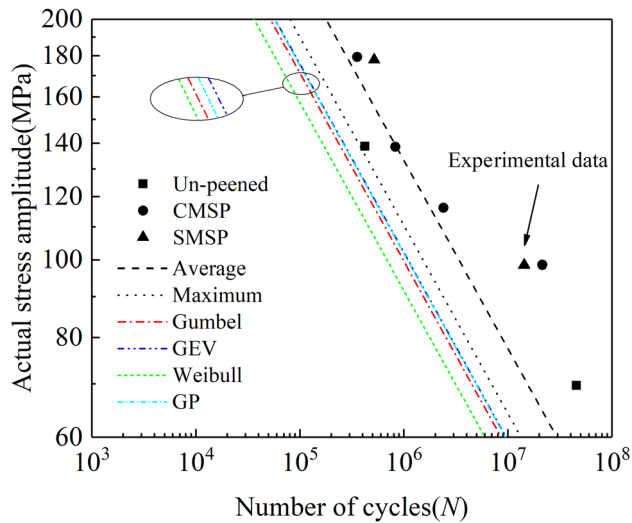


Fig. 13 $S-N$ curves predicted by Eq 9

propagation of internal casting defects to the surface when the fatigue lives of the CMSP and SMSP specimens were predicted using the LEFM method. Thus, it was easy to explain why the predicted results for the CMSP and SMSP specimens were smaller than the experimental results. In addition, as discussed in Sects. 3.1–3.3, the depth of the affected layer of SMSP sample was larger than that of CMSP sample. Thus, the crack propagation inhibition effect was more significant, which resulted in the predicted lives of the SMSP specimens deviating more significantly from the experimental fatigue life. Moreover, based on the corresponding initial crack length when the failure probability was 99% listed in Table 3, the $S-N$ curves of the UP sample were calculated, as shown in Fig. 13. It can be found that when the failure probability was 99%, all four distribution

functions could provide conservative predictions. The predicted fatigue strengths at 5×10^7 cycles had the following relationship: GEV > GP > Gumbel > Weibull.

4.2 Fatigue Life Prediction for Samples with Surface Crack Initiation

In addition to internal casting defects, a large portion of the failure modes also corresponded to surface crack initiation (68%), as listed in Table 2. Therefore, it was necessary to establish a fatigue life prediction model with the surface crack initiation. A modification relationship of the total strain life equation between the total strain amplitude and the number of loading cycles was proposed, while the elastic strain amplitude ϵ_e in the modification relationship considering the compressive residual stress on the surface after shot-peened treatments. The final form after the modification with the compressive residual stress is as Eq 10. A method for estimating the fatigue parameters of aluminum alloy materials using tensile strength σ_b based on an analysis of a large amount of test data for the aluminum alloy was proposed (Ref 58). Fatigue parameters of aluminum alloy estimated using the Meggiolaro method (Ref 58) are: $1.9 \sigma_b$ (σ'_f), -0.11 (b), 0.28 (ϵ'_f), and -0.66 (c), respectively. Here, σ_r in Eq 10 could be equivalent to take the mean value of equidistant points (0, 10, 20, 30, 40, 50, 60, 70, 80, 90, 100, 110, and 120 μm for CSP specimen; 0, 10, 20, 30, 40, 50, 60, and 70 μm for SMSP specimen) on the curve for the in-depth compressive residual stress, and the values of σ_r for the CSP and SMSP specimens were -127 and -106 MPa, respectively.

Using the Ramberg–Osgood function, the cyclic stress–strain curve can be described as follows:

$$\epsilon_a = \frac{\sigma_a}{E} + \left(\frac{\sigma_a}{K'} \right)^{1/n'} \quad (\text{Eq 18})$$

where K' is the cyclic hardening coefficient; n' is the cyclic hardening exponent; K' can be calculated using Eq 19, and n' can be determined using Eq 20.

$$K' = \frac{\sigma'_f}{(\epsilon'_f)^{n'}} \quad (\text{Eq 19})$$

$$n' = \frac{b}{c} \quad (\text{Eq 20})$$

The values of total strain amplitude ϵ_a for different values of loading stress σ_a can be determined by combining Eq 18–20 and the Meggiolaro method (Ref 58) for estimating the fatigue parameters. Then, the values of fatigue life N_f under different loading stresses can be determined with the values of total strain amplitude ϵ_a and σ_r for different shot-peened treatments using Eq 10. Figure 14 shows a comparison of the predicted and experimental fatigue lives. It can be seen that most of the predicted results were 2–3 times the dispersion band. In general, the predicted results were in good agreement with the experimental results. It was slightly inadequate that the predicted results under high stress levels in the CSP and UP samples differed greatly from the experimental results. Figure 15 shows the Manson–Coffin strain life curve calculated by

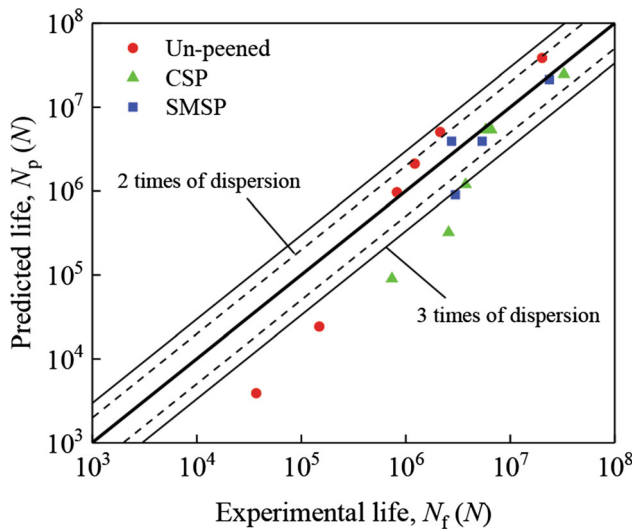


Fig. 14 Comparison of predicted and experimental fatigue lives based on Morrow model

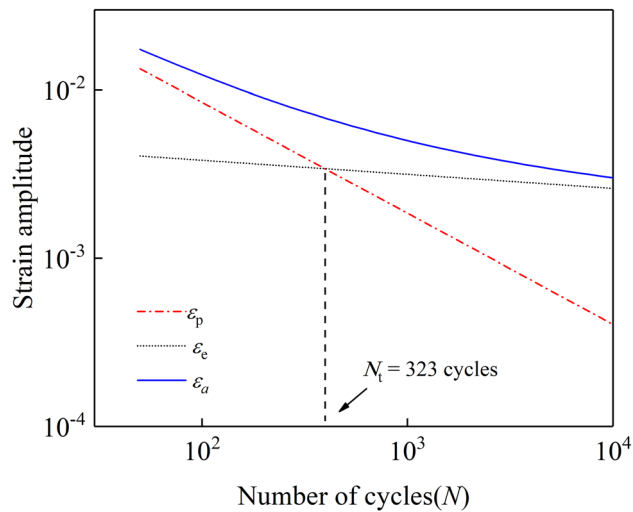


Fig. 15 Manson-Coffin strain life curve

Eq 10. The intersection point of elastic strain amplitude ϵ_e and plastic strain amplitude ϵ_p corresponded to transition life N_t , which was 398 cycles. It can be seen that the fatigue lives of all the samples were much longer than transition life N_t . Thus, the cyclic deformation was mainly elastic. Therefore, compared with the ductility of the material, strength played a more important role in the fatigue failure resistance.

5. Conclusions

In this study, Al-7Si-0.3Mg casting aluminum alloy specimens were subjected to CSP and fatigue testing. In addition, the influences of different shot-peened treatments (CSP, CMSP, and SMSP) on the fatigue strength were investigated. The following main conclusions could be drawn:

1. Compared with CMSP and SMSP, a larger surface compressive residual stress and deeper depth for the layer af-

ected by the residual stress could be achieved using CSP. The hardening effect follows the relationship: CSP > SMSP > CMSP. However, the surface roughness was also significantly increased, and the integrity was significantly worse than that after CMSP and SMSP.

2. The three different shot-peened treatments could effectively improve the fatigue strength of Al-7Si-0.3Mg casting aluminum alloy compared with the UP samples, and the fatigue limits of the CSP, CMSP and SMSP samples at 5×10^7 cycles increased by 50, 33, and 33%, respectively. Thus, the CSP treatment is recommended to achieve a better improvement on fatigue strength.
3. Under the same loading stress, the relaxation rate for the compressive residual stress on the surface of the CSP specimen was higher than those of the CMSP and SMSP samples.
4. The different values for the residual stress, depth of the affected layer, and roughness introduced by the different shot-peened treatments caused a change in the fatigue fracture mechanism.
5. The fatigue lives of the samples with the internal casting defects failure mode were predicted using LEFM, while those for samples with the surface crack initiation failure mode were predicted using the modified Morrow model considering residual stress, with the predictions in good agreement with the experimental results.

Acknowledgments

This work was supported by National Natural Science Foundation of China (No. 51675445, U1534209) and Independent Research Project of State Key Laboratory of Traction Power (No. 2019TPL-T06).

References

1. Y.H. Fan, S.H. Liu, and Y. Wang, Application of EN AC-ALSi7Mg0.6 Aluminum Alloy for Railway Contact Network, *Hot Work. Technol.*, 2015, 7, p 108–109
2. M. Benedetti, V. Fontanari, P. Scardi, C.A. Ricardo, and M. Bandini, Reverse Bending Fatigue of Shot Peened 7075-T651 Aluminium Alloy: The Role of Residual Stress Relaxation, *Int. J. Fatigue*, 2009, 31(8–9), p 1225–1236
3. J. González, S. Bagherifard, M. Guagliano, and I.F. Pariente, Influence of Different Shot Peening Treatments on Surface State and Fatigue Behaviour of Al 6063 Alloy, *Eng. Fract. Mech.*, 2017, 185, p 72–81
4. X. Li, J. Zhang, B. Yang, J. Zhang, M. Wu, and L. Lu, Effect of Micro-shot Peening, Conventional Shot Peening and Their Combination on Fatigue Property of EA4T Axle Steel, *J. Mater. Process. Technol.*, 2020, 275, p 116320
5. S. Kikuchi, Y. Nakamura, K. Nambu, and M. Ando, Effect of Shot Peening Using Ultra-Fine Particles on Fatigue Properties of 5056 Aluminum Alloy under Rotating Bending, *Mater. Sci. Eng. A*, 2016, 652, p 279–286
6. K. Oguri, Fatigue Life Enhancement of Aluminum Alloy for Aircraft by Fine Particle Shot Peening (FPSP), *J. Mater. Process. Technol.*, 2011, 211(8), p 1395–1399
7. K. Oguri, T. Sekigawa, and A. Inoue, Fatigue Property Enhancement of Aircraft Metallic Materials by Fine Particle Shot Peening, *Bull. Jpn. Inst. Met.*, 2008, 47, p 553–559
8. D.J. Chadwick, S. Ghanbari, D.F. Bahr, and M.D. Sangid, Crack Incubation in Shot Peened AA7050 and Mechanism for Fatigue Enhancement, *Fatigue Fract. Eng. Mater. Struct.*, 2018, 41(1), p 71–83
9. H. Luong and M.R. Hill, The Effects of Laser Peening on High-Cycle Fatigue in 7085-T7651 Aluminum Alloy, *Mater. Sci. Eng. A*, 2008, 477(1–2), p 208–216

10. E. Maleki, O. Unal, and K.R. Kashyzadeh, Efficiency Analysis of Shot Peening Parameters on Variations of Hardness, Grain Size and Residual Stress via Taguchi Approach, *Met. Mater. Int.*, 2019, **25**, p 1–12
11. J.H. Zhang, X.Q. Cheng, Q.X. Xia, and J.Y. Li, Influence of Laser Shot Peening Parameters on the Surface Hardness and Roughness of 7075 Aluminum Alloy. In *Materials Science Forum* (Vol. 920, pp. 83–88). Trans Tech Publications (2018)
12. R. Ramos, N. Ferreira, J.A.M. Ferreira, C. Capela, and A.C. Batista, Improvement in Fatigue Life of Al 7475-T7351 Alloy Specimens by Applying Ultrasonic and Microshot Peening, *Int. J. Fatigue*, 2016, **92**, p 87–95
13. A. Turnbull, E.R. De Los Rios, R.B. Tait, C. Laurant, and J.S. Boabaid, Improving the Fatigue Crack Resistance of Waspaloy by Shot Peening, *Fatigue Fract. Eng. Mater. Struct.*, 1998, **21**(12), p 1513–1524
14. M.Z. Wu, J.W. Zhang, G.M. Mei, J.X. Zhang, and X. Li, Effects of Fine Particle Shot Peening Treatment on Fatigue Properties of Al-7Si-0.3Mg Alloy, *J. Mater. Eng. Perform.*, 2019, **28**(5), p 2600–2609
15. N. Li, H.T. Li, J.Y. Zhou, H.T. Liu, C.K. Liu, and S.Y. Qu, Influence of Different Surface Treatments on Fatigue Life of 7050 Al Alloy, *Mater. Sci. Forum*, 2019, **944**, p 142–148
16. K. Dalaei, B. Karlsson, and L.E. Svensson, Stability of Shot Peening Induced Residual STRESSES and Their Influence on Fatigue Lifetime, *Mater. Sci. Eng. A*, 2011, **528**(3), p 1008–1015
17. Kodama, S., The Behavior of Residual Stress during Fatigue Stress Cycles, in *Proceedings of the International Conference on Mechanical Behavior of Metals II, Society of Material Science, Kyoto*, 1972, vol. 2, pp. 111–118
18. P. Li, P.D. Lee, D.M. Maijer, and T.C. Lindley, Quantification of the Interaction Within Defect Populations on Fatigue Behavior in an Aluminum Alloy, *Acta Mater.*, 2009, **57**(12), p 3539–3548
19. I. Serrano-Munoz, J.Y. Buffiere, R. Mokso, C. Verdu, and Y. Nadot, Location, Location & Size: Defects Close to Surfaces Dominate Fatigue Crack Initiation, *Sci. Rep.*, 2017, **7**, p 45239
20. S.E. Stanzl-Tschegg, H.R. Mayer, A. Beste, and S. Kroll, Fatigue and Fatigue Crack Propagation in AlSi7Mg Cast Alloys under In-Service Loading Conditions, *Int. J. Fatigue*, 1995, **17**(2), p 149–155
21. Q.G. Wang, D. Apelian, and D.A. Lados, Fatigue Behavior of A356-T6 Aluminum Cast Alloys: Part I—Effect of Casting Defects, *J. Light Met.*, 2001, **1**(1), p 73–84
22. M.E. Seniw, M.E. Fine, E.Y. Chen, M. Meshii, and J. Gray, *Relation of Defect Size and Location to Fatigue Failure in Al Alloy A356 Cast Specimens* (No. CONF-970980-). The Minerals, Metals and Materials Society, 1997, Warrendale, PA
23. S. Jana, R.S. Mishra, J.B. Baumann, and G. Grant, Effect of Friction Stir Processing on Fatigue Behavior of an Investment Cast Al-7Si-0.6Mg Alloy, *Acta Mater.*, 2010, **58**(3), p 989–1003
24. A. Rotella, Y. Nadot, M. Piellard, R. Augustin, and M. Fleuriot, Fatigue Limit of a Cast Al-Si-Mg Alloy (A357-T6) with Natural Casting Shrinkages Using ASTM Standard X-Ray Inspection, *Int. J. Fatigue*, 2018, **114**, p 177–188
25. J. Zhang, W. Li, H. Wang, Q. Song, L. Lu, W. Wang, and Z. Liu, A Comparison of the Effects of Traditional Shot Peening and Micro-shot Peening on the Scuffing Resistance of Carburized and Quenched Gear Steel, *Wear*, 2016, **368**, p 253–257
26. J.W. Zhang, L.T. Lu, K. Shiozawa, X.L. Shen, H.F. Yi, and W.H. Zhang, Analysis on Fatigue Property of Microshot Peened Railway Axle Steel, *Mater. Sci. Eng. A*, 2011, **528**(3), p 1615–1622
27. J.C. Kim, S.K. Cheong, and H. Noguchi, Evolution of Residual Stress Redistribution Associated with Localized Surface Microcracking in Shot-Peened Medium-Carbon Steel during Fatigue Test, *Int. J. Fatigue*, 2013, **55**, p 147–157
28. B. Skallerud, T. Iveland, and G. Härkegård, Fatigue Life Assessment of Aluminum Alloys with Casting Defects, *Eng. Fract. Mech.*, 1993, **44**(6), p 857–874
29. S. Barter, L. Molent, N. Goldsmith, and R. Jones, An Experimental Evaluation of Fatigue Crack Growth, *Eng. Fail. Anal.*, 2005, **12**(1), p 99–128
30. Q.G. Wang, P.N. Crepeau, C.J. Davidson, and J.R. Griffiths, Oxide Films, Pores and the Fatigue Lives of Cast Aluminum Alloys, *Metal. Mater. Trans. B*, 2006, **37**(6), p 887–895
31. B.R. Crawford, C. Loader, A.R. Ward, C. Urbani, M.R. Bache, S.H. Spence, and A.J. Stonham, The EIFS Distribution for Anodized and Pre-corroded 7010-T7651 under Constant Amplitude Loading, *Fatigue Fract. Eng. Mater. Struct.*, 2005, **28**(9), p 795–808
32. Y.K. Gao and X.R. Wu, Experimental Investigation and Fatigue Life PREDICTION for 7475-t7351 Aluminum Alloy With and Without Shot Peening-Induced Residual Stresses, *Acta Mater.*, 2011, **59**(9), p 3737–3747
33. A.J. McEvily, Current Aspects of Fatigue, *Met. Sci.*, 1977, **11**(8–9), p 274–284
34. H.U. Staal and J.D. Elen, Crack Closure and Influence of Cycle Ratio R on Fatigue Crack Growth in Type 304 Stainless Steel at Room Temperature, *Eng. Fract. Mech.*, 1979, **11**(2), p 275–283
35. V. Bachmann and D. Munz, Fatigue Crack Closure Evaluation with the Potential Method, *Eng. Fract. Mech.*, 1979, **11**(1), p 61–71
36. Y. Murakami, and M. Endo, Effects of Hardness and Crack Geometries on $\mu\text{C}/\text{th}$ of Small Cracks Emanating from Small Defects, 1986
37. Y. Murakami, *Metal Fatigue: Effects of Small Defects and Nonmetallic Inclusions*, vol. 70(7), Elsevier, London, 2002, p 1197–1200
38. Y. Murakami and E. Masahiro, Quantitative Evaluation of Fatigue Strength of Metals Containing Various Small Defects or Cracks, *Eng. Fract. Mech.*, 1983, **17**(1), p 1–15
39. Y. Murakami, T. Toriyama, and E.M. Coudert, Instructions for a New Method of Inclusion Rating and Correlations with the Fatigue Limit, *J. Test. Eval.*, 1994, **22**(4), p 318–326
40. S. Beretta and Y. Murakami, Statistical Analysis of Defects for Fatigue Strength Prediction and Quality Control of Materials, *Fatigue Fract. Eng. Mater. Struct.*, 1998, **21**(9), p 1049–1065
41. H. Mayer, M. Papakyriacou, B. Zettl, and S.E. Stanzl-Tschegg, Influence of Porosity on the Fatigue Limit of Die Cast Magnesium and Aluminium Alloys, *Int. J. Fatigue*, 2003, **25**(3), p 245–256
42. H. Mayer, M. Papakyriacou, B. Zettl, and S. Vacic, Endurance Limit and Threshold Stress Intensity of Die Cast Magnesium and Aluminium Alloys at Elevated Temperatures, *Int. J. Fatigue*, 2005, **27**(9), p 1076–1088
43. P. White, L. Molent, and S. Barter, Interpreting Fatigue Test Results Using a Probabilistic Fracture Approach, *Int. J. Fatigue*, 2005, **27**(7), p 752–767
44. M. Tiryakioglu, Statistical Distributions for the Size of Fatigue-Initiating Defects in Al-7%Si-0.3%Mg Alloy Castings: A Comparative Study, *Mater. Sci. Eng. A*, 2008, **497**(1-2), p 119–125
45. S.S. Manson, *Behavior of Materials under Conditions of Thermal Stress*, vol. 2933, 1953, National Advisory Committee for Aeronautics
46. L.F. Coffin, Jr., A Study of the Effects of Cyclic Thermal Stresses on a Ductile Metal, *Trans. Am. Soc. Mech. Eng. N. Y.*, 1954, **76**, p 931–950
47. J. Morrow, *Fatigue Design Handbook*, *Adv. Eng.*, 1968, **4**, p 21–29
48. M.Z. Wu, J.W. Zhang, Y.B. Zhang et al., Effects of Mg Content on the Fatigue Strength and Fracture Behavior of Al-Si-Mg Casting Alloys, *J. Mater. Eng. Perform.*, 2018
49. M.T.A. El-Khair, Microstructure Characterization and Tensile Properties of Squeeze-Cast AlSiMg ALLOYS, *Mater. Lett.*, 2005, **59**(8/9), p 894–900
50. ASM International. Handbook Committee. *ASM Handbook*, vol. 19. ASM international, 1990
51. SAE Standard, J443—Procedures for Using Standard Shot Peening Test Strip, 2003
52. SAE international, Shot Peening Coverage Determination, SAE J2277, 2013
53. J. Lin, N. Ma, Y. Lei, and H. Murakawa, Measurement of Residual Stress in Arc Welded Lap Joints by $\cos\alpha$ X-Ray Diffraction Method, *J. Mater. Process. Technol.*, 2017, **243**, p 387–394
54. M.G. Moore and W.P. Evans, *Mathematical Correction for Stress in Removed Layers in X-Ray Diffraction Residual Stress Analysis* (No. 580035). SAE Technical Paper, 1958
55. Y.L. Lee, J. Pan, R.B. Hathaway, and M. Barkey, *Fatigue Testing and Analysis: Theory and Practice*, Elsevier, Butterworth-Heinemann, 2005
56. A. Khalili and K. Kromp, Statistical Properties of Weibull Estimators, *J. Mater. Sci.*, 1991, **26**(24), p 6741–6752
57. J.Z. Yi, P.D. Lee, T.C. Lindley, and T. Fukui, Statistical Modeling of Microstructure and Defect Population Effects on the Fatigue Performance of Cast A356-T6 Automotive Components, *Mater. Sci. Eng. A*, 2006, **432**(1–2), p 59–68
58. M.A. Meggiolaro and J.T.P. Castro, Statistical Evaluation of Strain-Life Fatigue Crack Initiation Predictions, *Int. J. Fatigue*, 2004, **26**(5), p 463–476

Publisher's Note Springer Nature remains neutral with regard to jurisdictional claims in published maps and institutional affiliations.